

Locally Divergence-Free Discontinuous Galerkin Methods for MHD Equations

Fengyan Li¹ and Chi-Wang Shu¹

Abstract

In this paper, we continue our investigation of the locally divergence-free discontinuous Galerkin method, originally developed for the linear Maxwell equations in [11], to solve the nonlinear ideal magnetohydrodynamics (MHD) equations. The distinctive feature of such methods is the use of approximate solutions that are exactly divergence-free inside each element for the magnetic field. As a consequence, this method has a smaller computational cost than the traditional discontinuous Galerkin method with standard piecewise polynomial spaces. We formulate the divergence-free discontinuous Galerkin method for the MHD equations and perform extensive one and two dimensional numerical experiments for both smooth solutions and solutions with discontinuities. Our computational results demonstrate that the divergence-free discontinuous Galerkin method, with a reduced cost comparing to the traditional discontinuous Galerkin method, can maintain the same accuracy for smooth solutions and can enhance the numerical stability of the scheme and reduce certain nonphysical features in some of the test cases.

Keywords: Discontinuous Galerkin method, divergence-free solutions, magnetohydrodynamics (MHD) equations

¹Division of Applied Mathematics, Brown University, Providence, RI 02912. E-mail: fengyan-l@dam.brown.edu, shu@dam.brown.edu. Research supported by ARO grant DAAD19-00-1-0405, NSF grant DMS-0207451, NASA Langley grant NCC1-01035 and AFOSR grant F49620-02-1-0113.

1 Introduction

In this paper we continue our development of the locally divergence-free discontinuous Galerkin method, studied first in [11] jointly with Cockburn for solving the linear Maxwell equations, to solve the two dimensional nonlinear ideal magnetohydrodynamics (MHD) equations. The method can be applied to three dimensions with no essential difficulty, but we will not consider it in this paper.

The locally divergence-free discontinuous Galerkin method is based on the traditional discontinuous Galerkin methods equipped with TVD Runge-Kutta time discretization (RKDG) [9, 12, 13]. The distinctive feature of the locally divergence-free discontinuous Galerkin method is the use of approximate solutions that are exactly divergence-free inside each element for certain vectors which should be divergence-free according to the PDEs, for example the magnetic field in the MHD equations.

There are many partial differential equations with solutions which are divergence-free. Examples include the incompressible Euler and Navier-Stokes equations, the magnetohydrodynamics (MHD) equations, and the Maxwell equations. For some of the problems, such as the MHD equations and the Maxwell equations, the solutions of the PDE should automatically satisfy the divergence-free condition if the initial data is divergence-free, but it is widely known that negligence in dealing with the divergence-free condition numerically sometimes can lead to serious defects, see, e.g. [17, 20, 6].

Attempts have been made in the literature to enforce explicitly the divergence-free condition. In the following we will review some of the divergence cleaning techniques in the context of MHD equations.

One way for the divergence correction is by projection, which, based on “Hodge decomposition”, was first suggested by Brackbill and Barnes [6] in the context of MHD. The numerical magnetic field \mathbf{B} is projected into a zero divergence vector space and the projected \mathbf{B} is used in the next time step. To implement this, usually a Poisson equation needs to be solved. Another method is Powell’s source term formulation [22], which is derived from

the physical laws if $\nabla \cdot \mathbf{B}$ is not used. Source terms proportional to $\nabla \cdot \mathbf{B}$ are added to the equations, which makes the system well behaved but non-conservative. For MHD equations, there is also the generalized Lagrange multiplier method, which was proposed by Dedner et al. [15]. With this method, the divergence errors could be transported to the domain boundaries with certain speed and damped at the same time.

Another approach, often referred to as “constrained transport methods”, was first brought up by Yee [32] in the electromagnetics, and then adapted to MHD equations by Brecht et al. [7], Evans and Hawley [16], Stone and Norman [29], etc. In this approach, a staggered mesh is used, and a suitably defined discrete approximation to the divergence of the solution can be maintained exactly zero. This method has been further developed recently by combining with the higher order Godunov type schemes by Dai and Woodward [14], Ryu et al. [25], Balsara and Spicer [5] etc. In [3, 4], Balsara developed such divergence-free reconstruction strategy in an adaptive mesh setting. In [30], Tóth compared some of the methods mentioned above and introduced the field/flux-interpolated central difference (CD) approaches, in which no staggered mesh is needed.

In the context of Stokes equations and the stationary Navier-Stokes equations, Baker et al. [2, 19] introduced a discontinuous Galerkin method by using an interior penalty method with locally divergence-free approximate solutions. Optimal error estimates were proven.

Similar to [11] for the two dimensional Maxwell equations, we follow the approach of Baker et al. [2, 19] and use the locally divergence-free piecewise polynomials as the solution space in the discontinuous Galerkin method to solve ideal MHD equations. Because the space is smaller, we can save in computational cost when using the locally divergence-free piecewise polynomial space compared with the standard piecewise polynomial space for the RKDG method. Theoretical study in [11], and numerical experiments in [11] and in this paper, indicate that this saving is not at the price of the degeneration of the solutions in stability and accuracy. On the contrary, both accuracy and stability can be enhanced in many cases. Compared with the Maxwell equations, the nonlinearity gives the solutions of MHD

equations much more complicated features. The RKDG method with locally divergence-free piecewise polynomial space can enhance numerical stability in several test cases, such as the Orszag-Tang vortex example and the shock reflection example. Also, nonphysical features are reduced in several test cases, such as the rotor example.

The paper is organized as follows. In Section 2, we describe the equations, introduce the locally divergence-free space and the numerical formulation of the algorithm. The numerical results are presented in Section 3. Concluding remarks are made in Section 4.

2 Equations and locally divergence-free discontinuous Galerkin method

The following two dimensional ideal MHD system will be considered:

$$\begin{aligned}
\partial_t \rho + \nabla \cdot (\rho \mathbf{u}) &= 0, \\
\partial_t(\rho \mathbf{u}) + \nabla \cdot \left[\rho \mathbf{u} \mathbf{u}^T + \left(p + \frac{1}{2} |\mathbf{B}|^2 \right) \mathcal{I} - \mathbf{B} \mathbf{B}^T \right] &= 0, \\
\partial_t \mathbf{B} + \nabla \cdot (\mathbf{u} \mathbf{B}^T - \mathbf{B} \mathbf{u}^T) &= 0, \\
\partial_t E + \nabla \cdot \left[\left(E + p + \frac{1}{2} |\mathbf{B}|^2 \right) \mathbf{u} - \mathbf{B} (\mathbf{u} \cdot \mathbf{B}) \right] &= 0,
\end{aligned} \tag{2.1}$$

Here ρ , p , $\mathbf{u} = (u_x, u_y, u_z)$, $\mathbf{B} = (B_x, B_y, B_z)$ and E denote the mass density, the hydrodynamic pressure, the velocity field, the magnetic field, and the total energy, respectively. The ratio of the specific heats is given by γ and $E = \frac{1}{2} \rho |\mathbf{u}|^2 + \frac{1}{2} |\mathbf{B}|^2 + \frac{p}{\gamma-1}$.

This is a hyperbolic system with a divergence-free solution \mathbf{B} for all time if initially it is divergence-free. The standard RKDG method for solving (2.1) would start with a triangulation \mathcal{T}_h of the domain Ω , with the element being denoted by K , the edge by e , and the outward unit normal by $\mathbf{n} = (n_1, n_2)$. We rewrite equations (2.1) in the conservative form

$$\mathbf{U}_t + \nabla \cdot \mathbf{F}(\mathbf{U}) = 0 \tag{2.2}$$

where

$$\mathbf{U} = (\rho, \rho u_x, \rho u_y, \rho u_z, B_x, B_y, B_z, E)^T.$$

$$F_1(\mathbf{U}) = (\rho u_x, \rho u_x^2 + p + \frac{1}{2}|\mathbf{B}|^2 - B_x^2, \rho u_x u_y - B_x B_y, \rho u_x u_z - B_x B_z, 0, u_x B_y - u_y B_x, \\ u_x B_z - u_z B_x, u_x(E + p + \frac{1}{2}|\mathbf{B}|^2) - B_x(u_x B_x + u_y B_y + u_z B_z))^T.$$

$$F_2(\mathbf{U}) = (\rho u_y, \rho u_y u_x - B_y B_x, \rho u_y^2 + p + \frac{1}{2}|\mathbf{B}|^2 - B_y^2, \rho u_y u_z - B_y B_z, u_y B_x - u_x B_y, 0, \\ u_y B_z - u_z B_y, u_y(E + p + \frac{1}{2}|\mathbf{B}|^2) - B_y(u_x B_x + u_y B_y + u_z B_z))^T.$$

We will also use $\mathbf{U}^p = (\rho, u_x, u_y, u_z, B_x, B_y, B_z, p)^T$ to denote the primitive variables for notational convenience.

Following the usual definition of discontinuous Galerkin methods for conservation laws, e.g. [9, 12], we obtain the RKDG formulation for (2.2): find $\mathbf{U}_h \in \mathbf{V}_h$, such that

$$\int_K \mathbf{U}_h \cdot \mathbf{v} d\mathbf{x} + \sum_{e \in \partial K} \int_e \mathbf{h}_{e,K}(\mathbf{U}_h^{int(K)}, \mathbf{U}_h^{ext(K)}, \mathbf{n}_{e,K}) \cdot \mathbf{v} ds - \int_K \mathbf{F}(\mathbf{U}_h) \cdot \nabla \mathbf{v} d\mathbf{x} = 0, \quad \forall \mathbf{v} \in \mathbf{V}_h, \quad \forall K, \quad (2.3)$$

where \mathbf{V}_h is the solution space, which is the same as the test space and is given by

$$\mathbf{V}_h = \mathbf{V}_h^k = \left\{ \mathbf{v} : \mathbf{v}|_K \in \mathbf{P}^k(K), \left(\frac{\partial v_5}{\partial x} + \frac{\partial v_6}{\partial y} \right) |_K = 0, \forall K \right\}, \quad (2.4)$$

where $\mathbf{P}^k(K) = (P^k(K))^8$, and $P^k(K)$ denotes the space of polynomials in K of degree at most k . By this definition, we will have solution spaces which contain magnetic fields with zero divergence within each element. We call these spaces the locally divergence-free spaces, and call the discontinuous Galerkin methods with these solution spaces the locally divergence-free discontinuous Galerkin methods. Since this space is a subspace of the standard piecewise polynomial space, we could expect cost saving by using the locally divergence-free spaces. More precisely, the dimension of $\mathbf{V}_h^k|_K$ is $\frac{(k+1)(k+4)}{2} + 3(k+1)(k+2)$, which is approximately $\frac{7}{8}$ of $4(k+1)(k+2)$, the dimension of $(P^k(K))^8$. It is easy to write out local bases for $\{(v_5, v_6) : \mathbf{v} = \{v_i\}_{i=1}^8, \mathbf{v} \in \mathbf{V}_h^k\}$ within K . For example, if K is a rectangle, with center (x_i, y_j) , and width $\Delta x_i, \Delta y_j$, if we denote $\bar{X} = \frac{x-x_i}{\Delta x_i}, \bar{Y} = \frac{y-y_j}{\Delta y_j}$, one set of orthogonal bases would be, when $k = 1$,

$$\begin{pmatrix} 1 \\ 0 \end{pmatrix}, \begin{pmatrix} \Delta x_i \bar{X} \\ -\Delta y_j \bar{Y} \end{pmatrix}, \begin{pmatrix} \bar{Y} \\ 0 \end{pmatrix}, \begin{pmatrix} 0 \\ 1 \end{pmatrix}, \begin{pmatrix} 0 \\ \bar{X} \end{pmatrix}.$$

For $k = 2$, we need to add

$$\begin{pmatrix} \Delta x_i(12\bar{X}^2 - 1) \\ -24\Delta y_j\bar{X}\bar{Y} \end{pmatrix}, \begin{pmatrix} -24\Delta x_i\bar{X}\bar{Y} \\ \Delta y_j(12\bar{Y}^2 - 1) \end{pmatrix}, \begin{pmatrix} 12\bar{Y}^2 - 1 \\ 0 \end{pmatrix}, \begin{pmatrix} 0 \\ 12\bar{X}^2 - 1 \end{pmatrix}.$$

In general, the local bases $\{(v_5, v_6) : \mathbf{v} = \{v_i\}_{i=1}^8, \mathbf{v} \in \mathbf{V}_h^k\}$ in K could be generated by taking the *curl* of bases of $P^{k+1}(K)$.

In (2.3), $\mathbf{h}_{\mathbf{e},\mathbf{K}}(\mathbf{v}^{int(K)}, \mathbf{v}^{ext(K)}, \mathbf{n}_{\mathbf{e},\mathbf{K}})$ is the numerical flux, which is an exact or approximate Riemann solver, consistent with $\mathbf{F}(\mathbf{U}) \cdot \mathbf{n}_{\mathbf{e},\mathbf{K}}$ and conservative,

$$\mathbf{h}_{e,K}(\mathbf{v}^{int(K)}, \mathbf{v}^{ext(K)}, \mathbf{n}_{e,K}) + \mathbf{h}_{e,K'}(\mathbf{v}^{int(K')}, \mathbf{v}^{ext(K')}, \mathbf{n}_{e,K'}) = 0, \quad K \cap K' = e,$$

here $\mathbf{v}^{int(K)}, \mathbf{v}^{ext(K)}$ are the limits of \mathbf{v} at interface e from the interior and exterior of K respectively. The one we will use in our numerical examples is the local Lax-Friedrichs flux,

$$\mathbf{h}_{e,K}(\mathbf{a}, \mathbf{b}, \mathbf{n}_{e,K}) = \frac{1}{2}[F(\mathbf{a}) \cdot \mathbf{n}_{e,K} + F(\mathbf{b}) \cdot \mathbf{n}_{e,K} - \alpha_{e,K}(\mathbf{b} - \mathbf{a})] \quad (2.5)$$

where $\alpha_{e,K}$ is an estimate of the largest absolute value of eigenvalues of the Jacobi $(\partial/\partial\mathbf{v})\mathbf{F}(\mathbf{v}) \cdot \mathbf{n}_{e,K}$ in the neighborhood of the edge e .

For discontinuous Galerkin methods applied to nonlinear systems such as (2.1), nonlinear limiters are often needed. In this paper we use the minmod TVB slope limiter by Shu [26] and Cockburn et al. [10, 12], which has a parameter M related to the magnitude of the second derivatives of the solution at smooth extrema. The limiter is implemented in local characteristic fields and we use the eigenvector system from [18]. It is a difficult task and an active research area to find good limiters for the discontinuous Galerkin methods in the presence of strong shocks, to obtain non-oscillatory results which are high order accurate in smooth regions. The emphasis of this paper is not on limiters, thus we will not discuss the optimal choice of limiters, rather we will use the minmod TVB slope limiter with suitable M (not necessarily optimal M) in the numerical tests. We do point out that sometimes the numerical results are sensitive to the choice of limiters. We refer the readers to [23, 24] for a recent effort in designing a new class of limiters for the discontinuous Galerkin method based on weighted essentially non-oscillatory (WENO) schemes.

3 Numerical Examples

In this section, we present the numerical results of the discontinuous Galerkin methods for one dimensional test problems using the standard piecewise P^k elements, and two dimensional test problems using both the standard piecewise P^k elements and locally divergence-free piecewise P^k elements, or just one of them if the results are similar, with $k = 1, 2$, namely the second and third order methods. We include the one dimensional examples here for the sake of completeness. By the same notation introduced in Section 2, the one dimensional system could be written as follows

$$\mathbf{U}_t + (F_1(\mathbf{U}))_x = 0,$$

and the divergence-free condition on the magnetic field reduces to $B_x = \text{constant}$. In all tests, the third order TVD Runge-Kutta time discretization [28] will be used. The time step will be dynamically determined by

$$\Delta t = \frac{C_{cfl} \min(\Delta x)}{\max(|u_x| + c_f)}$$

in the one dimensional case and by

$$\Delta t = C_{cfl} / \left\{ \frac{\max(|u_x| + c_f^x)}{\min(\Delta x)} + \frac{\max(|u_y| + c_f^y)}{\min(\Delta y)} \right\}$$

in the two dimensional case, where c_f (c_f^x, c_f^y) is the fast speed (in x, y direction) [18], the maxima (minima) are taken over all the computational cells, and the CFL number C_{cfl} is taken as 0.3 for the P^1 case and 0.18 for the P^2 case. Unless otherwise indicated, uniform rectangular meshes are used in the computation. The method, however, can be applied on arbitrary triangulations.

3.1 One dimensional Riemann problems

In this subsection, we solve standard one dimensional Riemann problems, see e.g. [18]. The first Riemann problem is given by

$$\mathbf{U}^p = \begin{cases} (1.000, 0, 0, 0, 0.75, +1, 0, 1.0) & \text{for } x < 0, \\ (0.125, 0, 0, 0, 0.75, -1, 0, 0.1) & \text{for } x > 0, \end{cases}$$

with $\gamma = 2$ on the computational domain $[-1, 1]$. Note that the hydrodynamic data are the same as the Sod's Riemann problem. This is the example used by Brio and Wu in [8] to show the formation of the compound wave in MHD.

The solution at $t = 0.2$ is shown in Figure 3.1, which includes the left moving waves: the fast rarefaction wave, the intermediate shock attached by a slow rarefaction wave; and the right moving waves: the contact discontinuity, a slow shock, and a fast rarefaction wave. The results obtained with 5000 cells serve as a reference in Figure 3.1. We can see that all the waves are resolved very well.

The second Riemann problem is

$$\mathbf{U}^p = \begin{cases} (1.000, 0, 0, 0, 0, +1, 0, 1000) & \text{for } x < 0, \\ (0.125, 0, 0, 0, 0, -1, 0, 0.10) & \text{for } x > 0, \end{cases}$$

with $\gamma = 2$. This problem is used to evaluate the code for high Mach number flow. If one regards the term $p + \frac{1}{2}|\mathbf{B}|^2$ as the “hydrodynamic pressure”, the system becomes a standard hydrodynamical Riemann problem, thus the exact solution could be easily obtained. The computational domain is taken to be $[-1, 1]$. The solution at $t = 0.012$ is shown in Figure 3.2, with the solid line as the exact solution.

In both problems we have applied the TVB minmod limiter with the TVB constant $M = 1$ in the local characteristic fields computed by the eigenvectors evaluated with the cell averages, see [9, 12] for the details of the implementation of such limiters. Our experience obtained from these one dimensional experiments is that the limiter should be used in the local characteristic fields rather than in the physical fields, in order to effectively control the spurious oscillations. This is consistent with the experience of hydrodynamic computations using the discontinuous Galerkin methods [10, 12].

3.2 Two dimensional examples

3.2.1 Examples with smooth solutions

The first example with smooth solutions is essentially a scalar problem, since there is only one nontrivial component ρ in the solution. The domain is taken to be $[0, 2\pi] \times [0, 2\pi]$ and $\gamma = 2$.

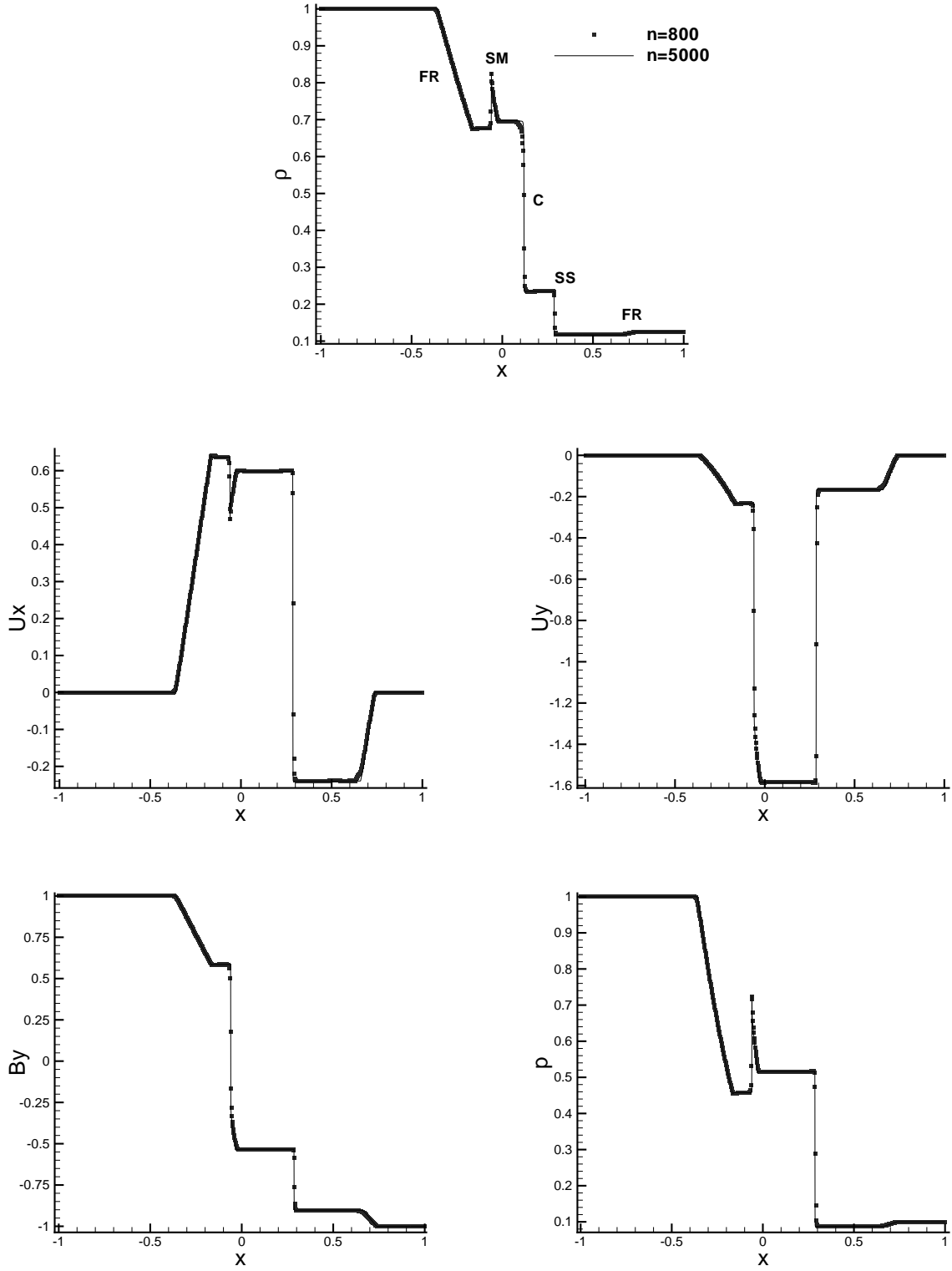


Figure 3.1: The first 1D Riemann example. P^2 with 800 cells (circles) on a background solid line computed with 5000 cells. $t = 0.2$ and $M = 1$. The symbol FR denotes a fast rarefaction wave; SM is a compound wave (an intermediate shock followed by a slow rarefaction wave); C is a contact discontinuity; SS is a slow shock. Top: ρ ; middle left: u_x ; middle right: u_y ; bottom left: B_y ; bottom right: p .

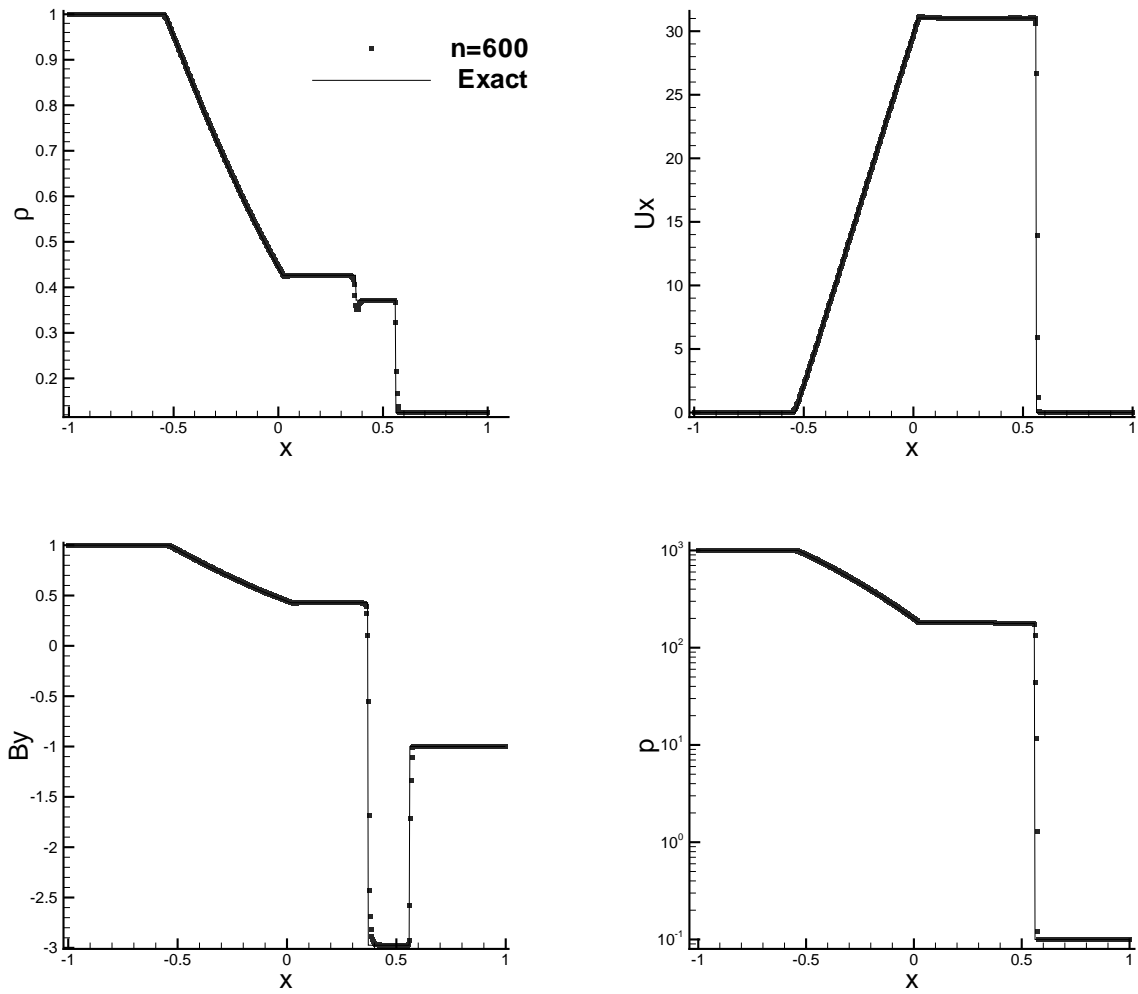


Figure 3.2: The second 1D Riemann example. P^2 with 600 cells (circles) on a background solid line of the exact solution. $t = 0.012$ and $M = 1$. Top left: ρ ; top right: u_x ; bottom left: B_y ; bottom right: p .

Table 3.1: L^2 and L^∞ errors and orders for ρ in the first 1D smooth example with initial condition $\rho(x, y) = 2 + \sin(x + y)$, $u_x = u_y = 1$, $p = 5$ at $t = 7$.

mesh	L^2 error	order	L^∞ error	order
P^1				
16×16	1.11E-01		1.77E-01	
32×32	1.84E-02	2.59	3.19E-02	2.47
64×64	3.36E-03	2.46	5.66E-03	2.50
128×128	7.29E-04	2.20	1.39E-03	2.02
P^2				
16×16	1.14E-03		8.34E-03	
32×32	1.44E-04	2.98	1.21E-03	2.78
64×64	1.81E-05	2.99	1.58E-04	2.94
128×128	2.27E-06	3.00	1.99E-05	2.99

The initial data is given by $\mathbf{U}^p = (\rho_0(x, y), 1, 1, 0, 0, 0, 5)$ with $\rho_0(x, y) = 2 + \sin(x + y)$. The periodic boundary condition is used. We compute until $t = 7$, after approximately two time periods. The exact solution for this problem is simply $\rho(x, y, t) = \rho_0(x - u_x t, y - u_y t)$ with other components remaining to be constants.

From Table 3.1, we can see that we obtain second order accuracy for the P^1 elements, and third order accuracy for the P^2 elements, both in L^2 and L^∞ norms, which are the optimal orders we expect. The drawback of this example is that only the hydrodynamical part of the system could be tested.

Next we look at a genuinely two dimensional vortex problem, which was originally suggested by Shu [27] in the hydrodynamical system, and was adapted to the MHD equations by Balsara [4]. The solution is a smooth vortex stably convected with the velocity field and the magnetic field. The unperturbed magnetohydrodynamic flow with $(\rho, u_x, u_y, B_x, B_y, p) = (1, 1, 1, 0, 0, 1)$ is initialized on the computational domain $[-10, 10] \times [-10, 10]$ with $\gamma = 5/3$. The vortex is introduced through the fluctuation in the velocity and magnetic fields given by

$$\begin{aligned}
(\delta u_x, \delta u_y) &= \frac{\eta}{2\pi} \nabla \times \exp\{0.5(1 - r^2)\} \\
(\delta B_x, \delta B_y) &= \frac{\xi}{2\pi} \nabla \times \exp\{0.5(1 - r^2)\},
\end{aligned}$$

where $r^2 = x^2 + y^2$, and the dynamical balance is obtained through the perturbation on pressure by

$$\delta p = (\xi^2(1 - r^2) - \eta^2) \frac{1}{8\pi^2} \exp(1 - r^2).$$

We use $\eta = 1$, $\xi = 1$ in our computation. Periodic boundary condition is used, the exact solution is just the one obtained from the initial configuration propagating with speed $(1, 1)$, or mathematically given by $\mathbf{U}^p(x, y, t) = \mathbf{U}_0^p(x - t, y - t)$.

Table 3.2 shows the L^2 errors and orders of accuracy for some representative components at $t = 20$. The errors are computed within $[-5, 5] \times [-5, 5]$ which contains the vortex. We can see that for both locally divergence-free piecewise P^1 elements and standard piecewise P^1 elements, second order accuracy is obtained. For the locally divergence-free piecewise P^2 elements, and standard piecewise P^2 elements, we obtain close to third order accuracy, and the order of accuracy with the locally divergence-free piecewise P^2 elements looks relatively closer to three. Also, the magnitude of the errors from the locally divergence-free space are comparable with the one obtained from the standard piecewise polynomial space with the same degree k .

3.2.2 Two dimensional Kelvin-Helmholtz instability

The Kelvin-Helmholtz instability can arise when two superposed fluids flow one over the other in a relative speed. Here we will use the discontinuous Galerkin methods to solve the two dimensional periodic model and convective model with transverse magnetic field configuration. See [18] and [31] for more details.

The initial stationary configuration is given by $\mathbf{U}^p = (1, u_{x0}, 0, 0, 0, 0, 1, 0.5)$ where $u_{x0}(x, y) = \tanh(y)$. At $t = 0$, a small perturbation is introduced to u_x by

$$\delta u_x = \begin{cases} -0.008 \sin(\frac{2\pi x}{\lambda}) / (1 + y^2), & \text{if } -\frac{\lambda}{2} < x < \frac{\lambda}{2} \\ 0, & \text{otherwise} \end{cases}$$

The computational domain is $[-\frac{L}{2}, \frac{L}{2}] \times [0, H]$. $\gamma = 2$. In the periodic model, $L = \lambda = 5\pi$, $H = 10$. The periodic boundary condition is used in the x direction, and the characteristic boundary condition is used for the top boundary. At $y = 0$, the boundary condition is

Table 3.2: L^2 errors and orders of accuracy in the 2D smooth vortex example computed within $[-5, 5] \times [-5, 5]$ at $t = 20$.

	ρ		u_x		B_x		p	
mesh	error	order	error	order	error	order	error	order
P^1								
32×32	3.89E-04		2.12E-02		2.11E-02		2.57E-03	
64×64	2.96E-04	0.39	8.56E-03	1.30	8.33E-03	1.34	1.22E-03	1.07
128×128	1.13E-04	1.39	2.08E-03	2.04	2.03E-03	2.04	2.92E-04	2.06
256×256	2.80E-05	2.01	4.65E-04	2.16	4.60E-04	2.14	6.04E-05	2.28
P^1 -LDF								
32×32	3.35E-04		2.06E-02		2.05E-02		2.63E-03	
64×64	2.47E-04	0.44	8.43E-03	1.29	8.06E-03	1.35	1.28E-03	1.04
128×128	9.99E-05	1.31	2.05E-03	2.04	1.94E-03	2.06	3.04E-04	2.07
256×256	2.63E-05	1.93	4.61E-04	2.16	4.51E-04	2.10	6.18E-05	2.30
P^2								
32×32	2.06E-04		1.04E-03		1.07E-03		3.63E-04	
64×64	2.40E-05	3.10	6.30E-05	4.05	9.36E-05	3.52	4.02E-05	3.17
128×128	3.08E-06	2.96	5.80E-06	3.44	1.53E-05	2.61	4.99E-06	3.01
256×256	6.07E-07	2.34	7.78E-07	2.90	2.65E-06	2.53	9.63E-07	2.37
512×512	1.06E-07	2.52	1.16E-07	2.75	4.28E-07	2.63	1.68E-07	2.52
P^2 -LDF								
32×32	2.05E-04		1.12E-03		1.14E-03		3.56E-04	
64×64	2.59E-05	2.98	6.44E-05	4.12	6.01E-05	4.24	4.27E-05	3.06
128×128	4.48E-06	2.53	6.48E-06	3.31	5.61E-06	3.42	7.35E-06	2.54
256×256	7.33E-07	2.61	8.87E-07	2.87	6.96E-07	3.01	1.20E-06	2.61
512×512	1.05E-07	2.80	1.19E-07	2.89	8.74E-08	2.99	1.72E-07	2.80

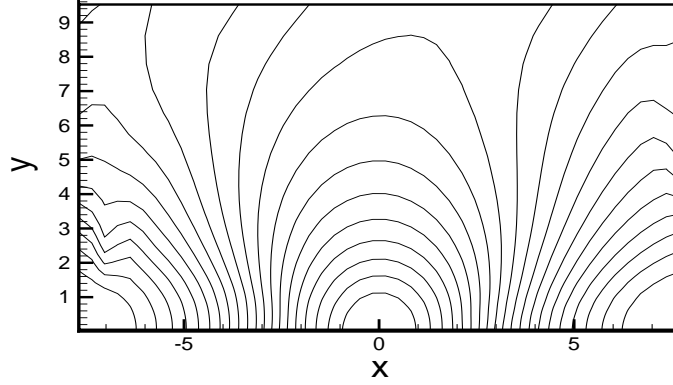


Figure 3.3: Kelvin-Helmholtz instability in the periodic model. 20 equally spaced contours of $\rho \in [0.82, 1.17]$. P^2 on a 48×30 mesh with Robert transform in the y direction. $M = 1$.

obtained from the following symmetry: under the transformation $(x, y) \rightarrow -(x, y)$, ρ , p , and B_z are symmetric and u_x , u_y are antisymmetric.

Since there are more features developed around $y = 0$, the Robert transform

$$y \leftarrow \frac{H \sinh(3y/H)}{\sinh(3)}$$

is used on the meshes in the y direction, which renders the mesh denser near $y = 0$ and coarser near $y = H$.

In the following computation, B_x , B_y are always zero, so there is no difference for this example to use piecewise P^k or locally divergence-free piecewise P^k . In Figure 3.3, we show the results at $t = 144$ with the TVB parameter $M = 1$. One can see the vortex flow generated from $y = 0$, off which there is some weak shock developed. Since there is no strong structure in this model, the computation is not very sensitive to the limiter parameter M .

Next, we check the numerical convergence of this method by looking at the cuts for ρ at $y = \frac{3}{10}H$ on uniform meshes: 48×30 , 80×100 and 100×150 . $M = 1$ and piecewise P^2 are used. In Figure 3.4, the convergence could be seen clearly, even around the rough area near the left boundary. Another way to see the convergence is to look at the time evolution

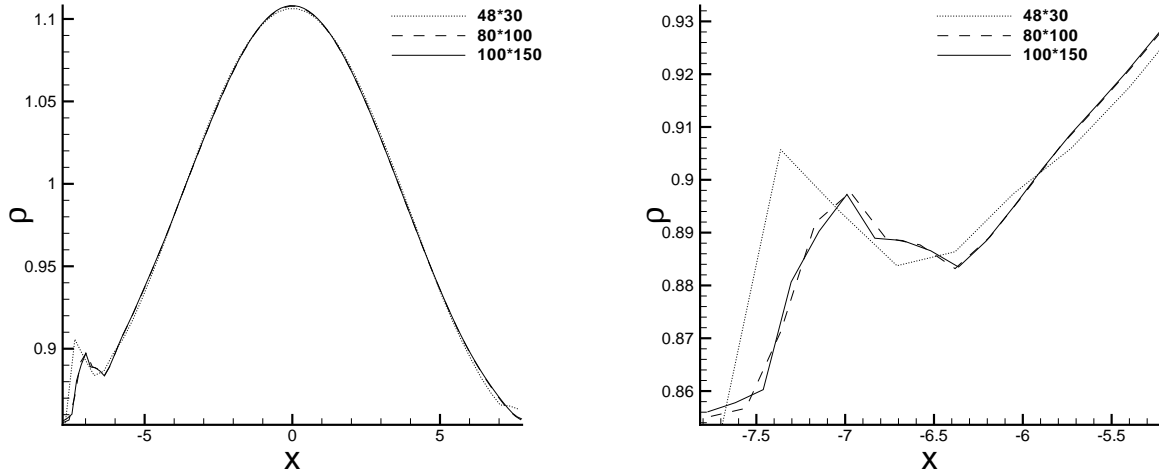


Figure 3.4: Kelvin-Helmholtz instability in the periodic model. Cuts of ρ at $y = \frac{3}{10}H$ to see convergence. P^2 on uniform meshes with $M = 1$. Dotted line: 48×30 ; dashed line: 80×100 ; solid line: 100×150 . Zoom-in plot is on the right.

curves of the total transverse kinetic energy over $[-\frac{L}{2}, \frac{L}{2}] \times [-H, H]$, which, for this example, is defined as $\int_{-\frac{L}{2}}^{\frac{L}{2}} \int_{-H}^H (\frac{1}{2} \rho u_y^2) dx dy$, see Figure 3.5. All the curves on the given meshes coincide with each other very well.

For the convective model, the same initial profile is used as in the periodic case. In contrast to the periodic model, the domain is enlarged, and the features developed as time evolves are allowed to convect away freely in the x direction. Using the same notation as in the periodic case, $L = 11\lambda = 55\pi$, $H = 20$. A 528×48 mesh is used with the same Robert transform in the y direction as in the periodic model. We observe the formation of larger vortices, and the shocks formed off these vortices are much stronger than the one found in the periodic system. Contour plots for density and pressure at $t = 120$ and $t = 145$ are shown in Figures 3.6 and 3.7. The overall features in this calculation are similar to those obtained in [18] and [31].

3.2.3 Two dimensional Riemann problem

The initial data for this two dimensional Riemann problem is chosen so that the solutions of the three of the four one dimensional Riemann problems are simple waves: if one denotes

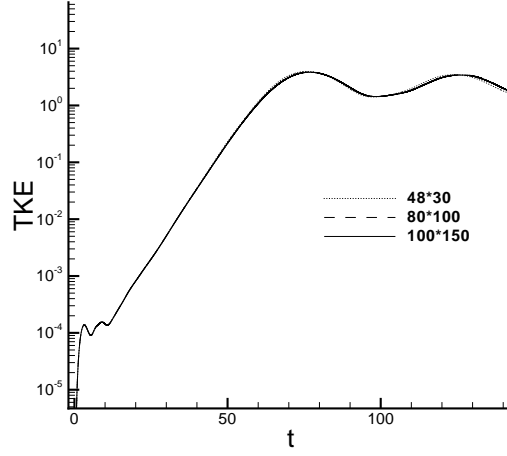


Figure 3.5: Kelvin-Helmholtz instability in the periodic model. Time evolution of the transverse kinetic energy to see convergence. P^2 on uniform meshes with $M = 1$. Dotted line: 48×30 ; dashed line: 80×100 ; solid line: 100×150 .

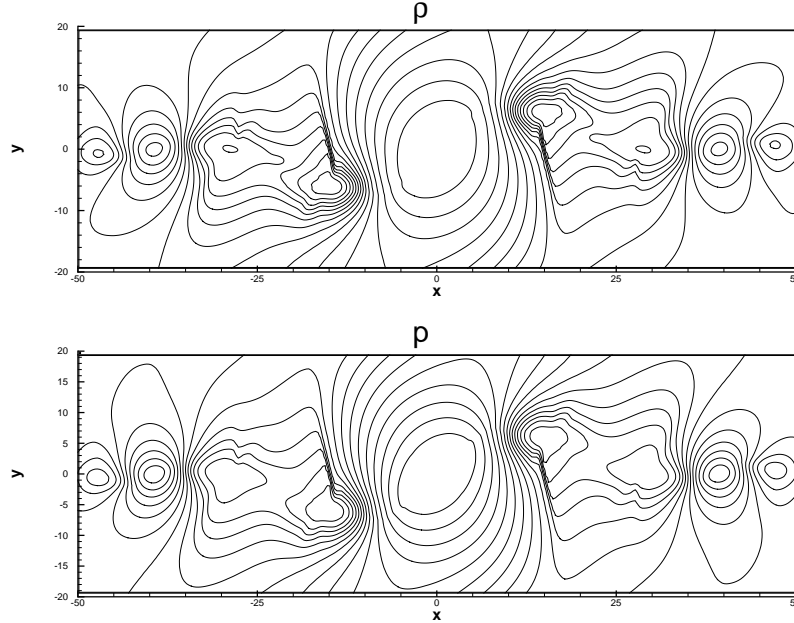


Figure 3.6: Kelvin-Helmholtz instability in the convective model at $t = 120$. 15 equally spaced contours for $\rho \in [0.67, 1.24]$ (top) and for $p \in [0.24, 0.79]$ (bottom). P^2 with $M = 0$ on a 528×96 mesh. Robert transform is used in the y direction.

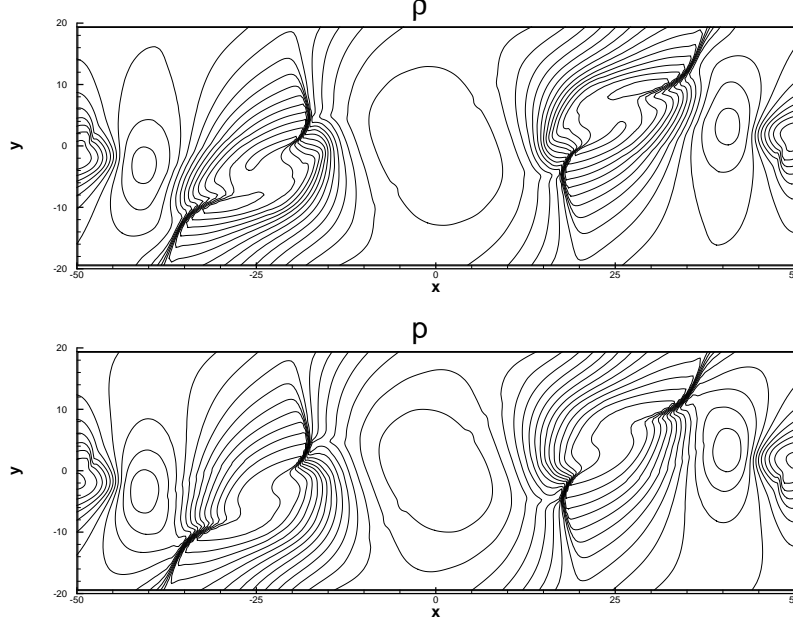


Figure 3.7: Kelvin-Helmholtz instability in the convective model at $t = 145$. 15 equally spaced contours for $\rho \in [0.44, 1.19]$ (top) and for $p \in [0.11, 0.73]$ (bottom). P^2 with $M = 0$ on a 528×96 mesh. Robert transform is used in the y direction.

the quadrants by Roman numbers counter-clockwisely starting from $\{(x, y) : x > 0, y > 0\}$, we have shocks for the problem II \leftrightarrow III and III \leftrightarrow IV and a rarefaction wave for I \leftrightarrow II (see [15]).

The initial condition is given as follows

$$\mathbf{U} = \begin{cases} (0.9308, 1.4557, -0.4633, & 0.0575, 0.3501, 0.9830, 0.3050, 5.0838) & \text{for } x > 0, y > 0 \\ (1.0304, 1.5774, -1.0455, & -0.1016, 0.3501, 0.5078, 0.1576, 5.7813) & \text{for } x < 0, y > 0 \\ (1.0000, 1.7500, -1.0000, & 0.0000, 0.5642, 0.5078, 0.2539, 6.0000) & \text{for } x < 0, y < 0 \\ (1.8887, 0.2334, -1.7422, & 0.0733, 0.5642, 0.9830, 0.4915, 12.999) & \text{for } x > 0, y < 0 \end{cases}$$

and the computational domain is taken to be $[-1, 1] \times [-1, 1]$. $\gamma = 5/3$. For the boundary conditions, instead of using the Dirichlet boundary conditions from numerical solutions of the one dimensional Riemann problems as in Dedner et al. [15], we simply use the Neumann boundary conditions.

Contours of B_x and B_y obtained with the standard piecewise P^2 elements and locally divergence-free piecewise P^2 elements are shown in Figure 3.8. We do not seem to have any problem in keeping B_y constant across the shock in the II \leftrightarrow III Riemann problem, or causing any strong distortions in the magnetic field components behind the rarefaction wave of the

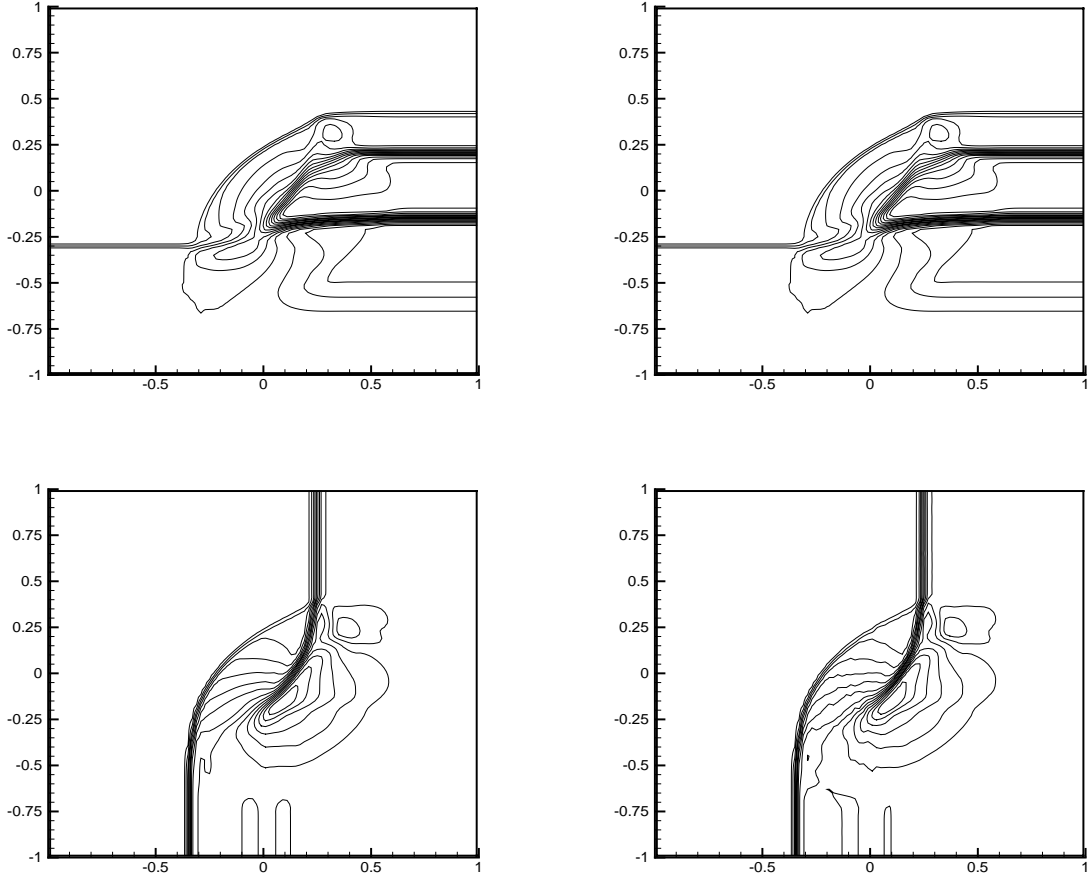


Figure 3.8: 2D Riemann problem. 15 equally spaced contours of $B_x \in [0.40, 1.16]$ (top) and of $B_y \in [0.54, 1.31]$ (bottom) at $t = 0.2$. 100×100 mesh size with $M = 1$. Left column: P^2 ; right column: P^2 -LDF.

I \leftrightarrow II Riemann problem, as for some methods in [15]. We also look at the similar cuts as in Figure 7 from [15], shown in our Figure 3.9, observing much smaller oscillations.

3.2.4 Orszag-Tang vortex example

In this subsection, we will consider the development of the Orszag-Tang vortex example [21], which is widely used as a test example in the literature because of the complex interaction between several shocks generated as the whole system evolves. Starting from a smooth state, after the transition period, the system will go to turbulence. The initial setup is the same as the one used in [18]

$$\mathbf{U}^p = (\gamma^2, -\sin y, \sin x, 0, -\sin y, \sin 2x, 0, \gamma),$$

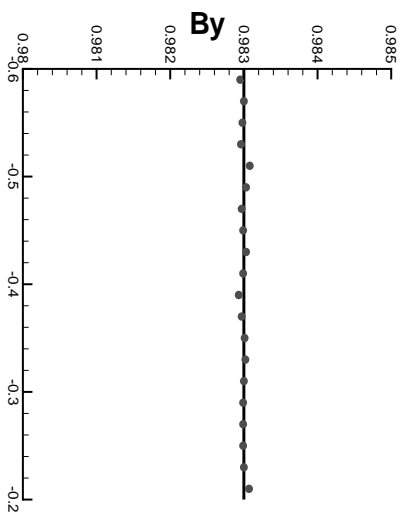
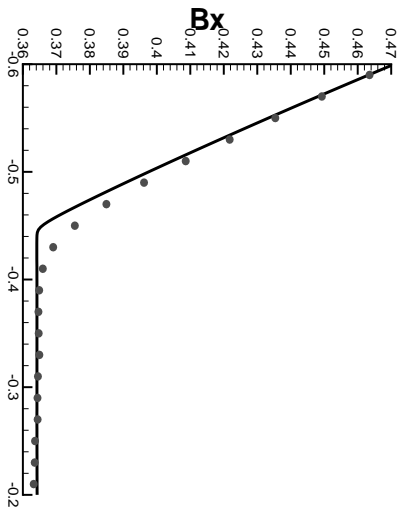
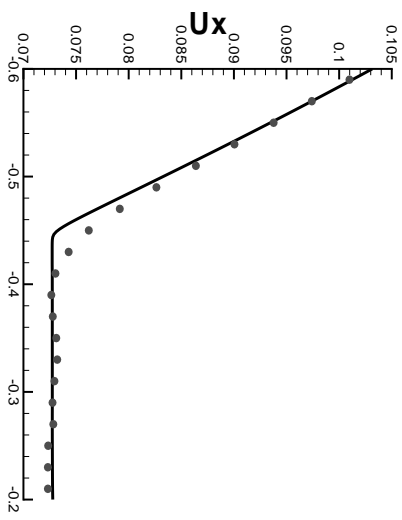
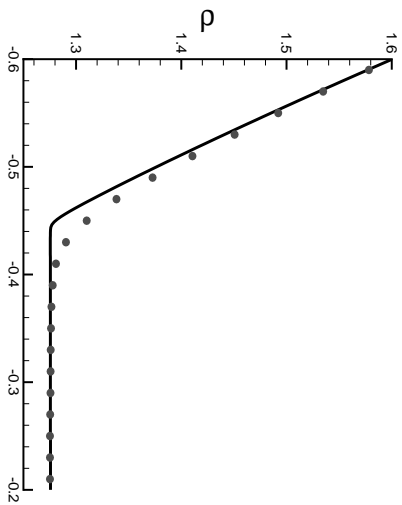


Figure 3.9: 2D Riemann problem. Cuts at $x = 0.93$ and $t = 0.2$ on 100×100 mesh with $M = 1$. Dotted line: P^2 -LDF; solid line: 1D reference results. Top left: ρ ; top right: u_x ; bottom left: B_x ; bottom right: B_y .

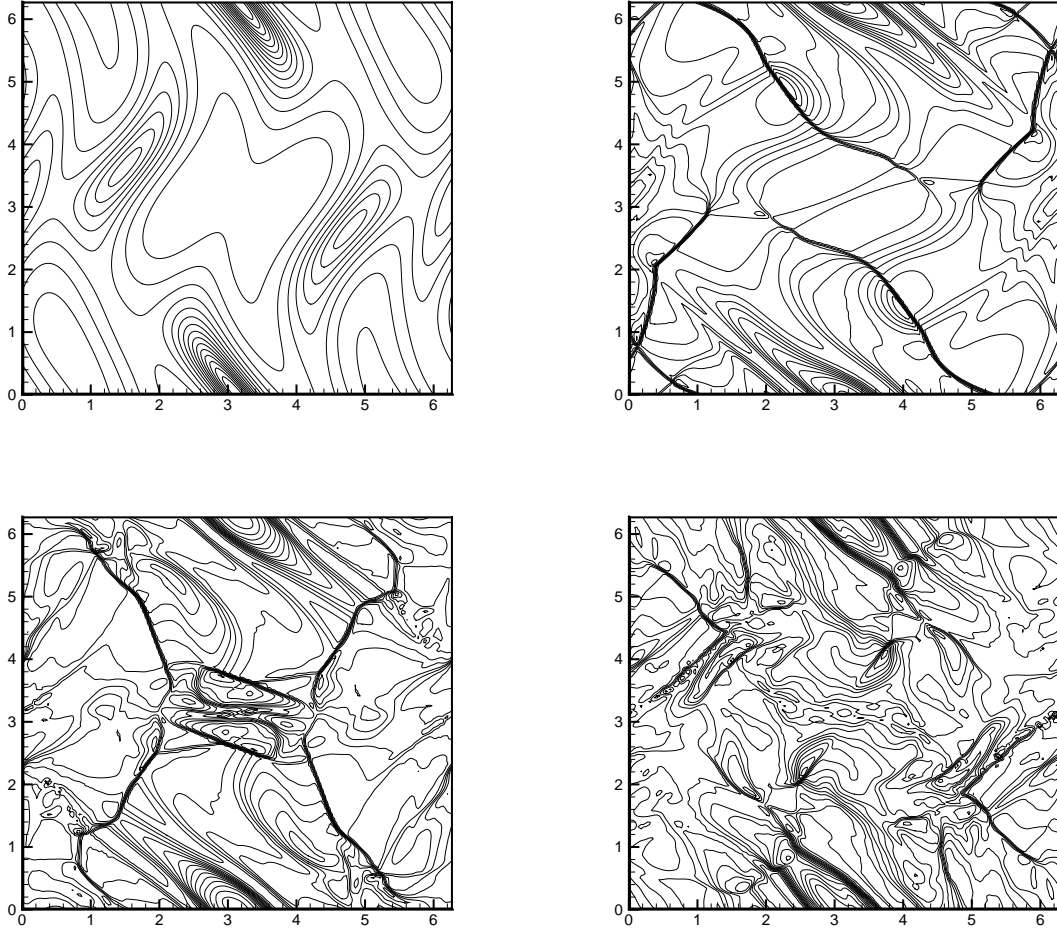


Figure 3.10: Orszag-Tang vortex example. The development of ρ with time: Top left: $t = 0.5$; top right: $t = 2$; bottom left: $t = 3$; bottom right: $t = 4$. 15 equally spaced contours with ranges $[2.33, 5.58]$, $[0.96, 5.87]$, $[1.56, 5.74]$ and $[1.33, 5.45]$, respectively. P^2 -LDF on 192×192 mesh with $M = 1$.

with $\gamma = 5/3$, and the computational domain is $[0, 2\pi] \times [0, 2\pi]$ with periodic boundary conditions.

The time development of density is shown in Figure 3.10. One can see that in the early stage, the solution is quite smooth. At $t = 2$, shocks have already appeared. At later time, for example, at $t = 3, 4$, the shocks interact with each other and the structure gets quite complicated.

During the computation, we notice that schemes with different solution spaces behave quite differently in numerical stability, in the sense that they are able to keep the computation

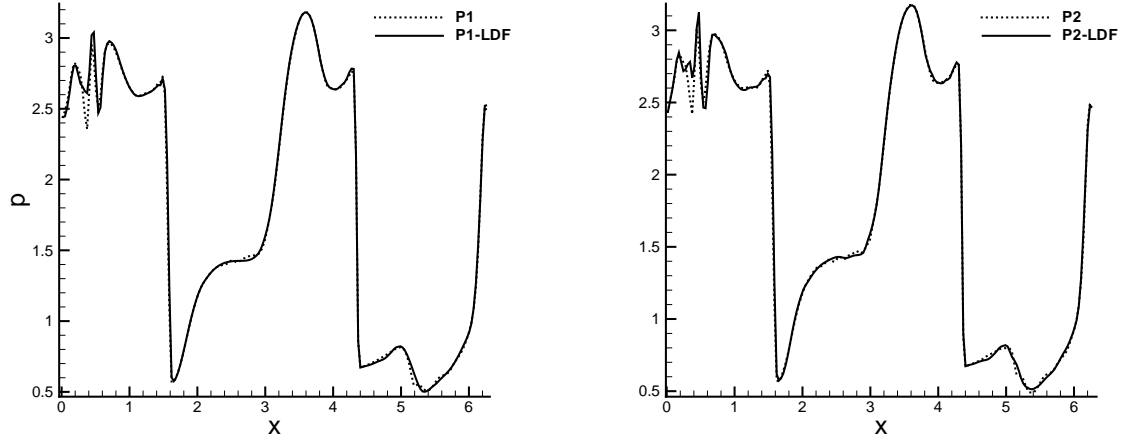


Figure 3.11: Orszag-Tang vortex example. The pressure distribution along $y = 0.625\pi$ on a 192×192 mesh at $t = 3$ with $M = 1$. Dotted line: standard P^k ; solid: P^k -LDF. Left: $k = 1$; right: $k = 2$.

from blowing up or delay the blowing up. For example, by using the 192×192 mesh with $M = 1$, computation with piecewise P^1 elements could reach $t = 3.45$, yet using locally divergence-free piecewise P^1 elements, we could do the computation at least until $t = 30$ (and it seems that the computation could go on forever). We do not have the same luck when $k = 2$, but still by using locally divergence-free piecewise P^2 elements the computation could go on until $t = 4.14$, instead of $t = 3.60$ when the piecewise P^2 elements are used. The stability problem with $k = 2$ seems to be related to the choice of limiters, which needs further investigation and will not be discussed further in this paper.

If we take a closer look, we find out that the formation of negative pressure is one factor for the numerical instability. During the computation, the locally divergence-free piecewise P^k space generally has a stronger self-healing ability when it encounters negative pressure, compared with the piecewise P^k space. One can also see the different behavior of these two types of spaces from the cuts of pressure in Figure 3.11: the locally divergence-free P^k elements always give a smoother curve than the standard piecewise P^k , and this can be confirmed by looking at the results on the refined mesh, see Figure 3.12.

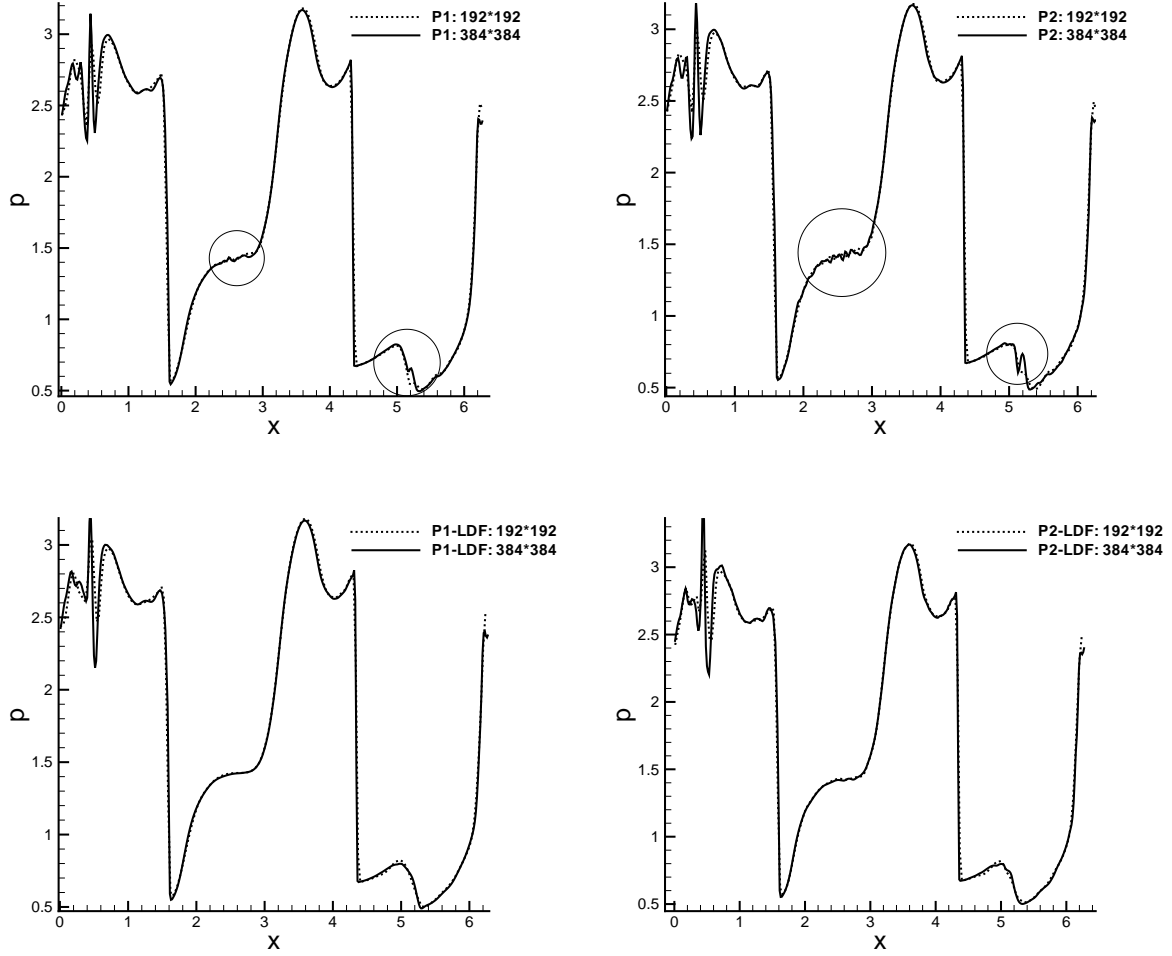


Figure 3.12: Orszag-Tang vortex example. The pressure distribution along $y = 0.625\pi$ on 192×192 (dotted line) and 384×384 (solid line) meshes at $t = 3$ with $M = 1$. Top: standard P^k ; bottom: P^k -LDF. Left: $k = 1$; right: $k = 2$.

3.2.5 Shock reflection

In this subsection, the shock reflection example suggested in [1] is considered. This problem was originally constructed such that a 29° reflected shock is the equilibrium solution across a Cartesian tube. The setup here is the same as in [15]. We take $[-1, 1] \times [-0.5, 0.5]$ as the computational domain, and $\gamma = 1.4$. If denote

$$\mathbf{U}_l^p = (1.0, 2.9, 0.0, 0.0, 0.5, 0.0, 0.0, 5/7),$$

$$\mathbf{U}_t^p = (1.4598, 2.7170, -0.4049, 0.0, 0.6838, -0.1019, 0.0, 1.2229),$$

then $\mathbf{U}^p = \mathbf{U}_l^p$ is used as the initial data, Dirichlet boundary conditions on top and left are $\mathbf{U}^p = \mathbf{U}_t^p$ and $\mathbf{U}^p = \mathbf{U}_l^p$, and the lower and right boundary conditions are taken as reflective and outgoing, respectively.

The results for density at $t = 2$ are shown in Figure 3.13 on a 100×100 mesh with $M = 1$. The result on the left is from the computation using standard piecewise P^2 elements, which is very oscillatory compared with the one using locally divergence-free piecewise P^2 elements. Similar oscillatory features were also observed in [1]. The oscillatory features using the standard piecewise P^k elements finally make the computation blow up. For example, for $k = 1$, the blowing up happens at $t=3.64$. Computation using locally divergence-free P^k could however continue stably.

To see what happens here, we plot the contours for ρ at different times in Figure 3.14. One could see that at early time, for example at $t = 0.2$ and $t = 0.4$, when the shock is not fully developed, the two solution spaces behave quite similarly. There are some small numerical structures around the top left corner, which is quite common in the computation of such problems. When time goes on, the situation is changed: in the case with the locally divergence-free solution space, those small numerical structures stemming out from the corner are slowly smoothed out, and convected away through the right boundary, so the whole computation moves on stably. For the standard piecewise P^k computation, however, there are small scale structures generated to the right of the shocks, for example at $t = 0.6$,

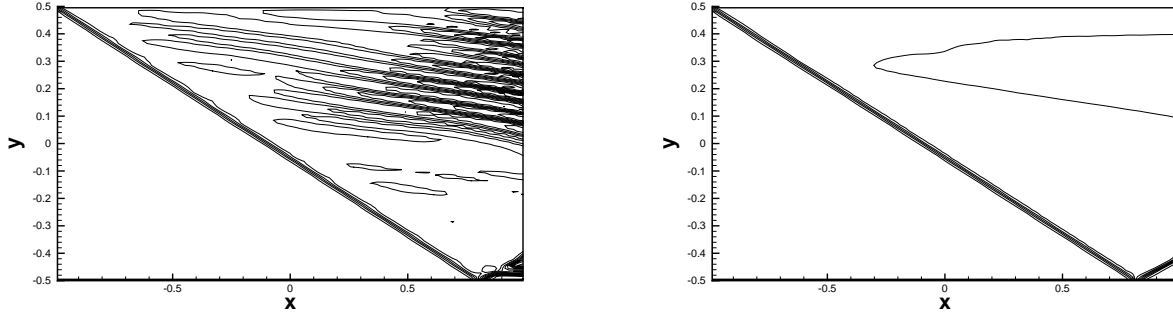


Figure 3.13: Shock reflection. 15 equally spaced contours of $\rho \in [1.86, 2.18]$ at $t = 2$ on 100×100 mesh with $M = 1$. Left: P^2 ; right: P^2 -LDF.

which accumulate, form oscillations and make the computation unstable eventually. What we see here is quite similar to what we have seen in the Orszag-Tang vortex example: the locally divergence-free space has some “smoothing” effect in the computation, which could enhance the stability of the scheme.

Moreover, the computation using the standard piecewise P^k is very sensitive to the limiter parameter M ; the larger M is, the earlier the computation blows up. As for the computation with locally divergence-free P^k , the parameter M has no apparent influence to the stability.

3.2.6 Rotor

In this subsection, we study the rotor example from [30].

The setup of this problem is as follows. There is a dense rotating disk of fluid located in the central area, while the ambient fluid is at rest. A “taper” function is used between these two areas, which helps to reduce initial transient.

The computational domain is taken as $[0, 1] \times [0, 1]$. $\gamma = 5/3$. The initial condition is given by

$$\mathbf{U}^p = (\rho_0, u_{x0}, u_{y0}, 0, 2.5/\sqrt{4\pi}, 0, 0, 0.5)$$

with

$$(\rho_0(\mathbf{x}), u_{x0}(\mathbf{x}), u_{y0}(\mathbf{x})) = \begin{cases} (10, -(y - 0.5)/r_0, (x - 0.5)/r_0), & \text{if } r < r_0 \\ (1 + 9f, -f \cdot (y - 0.5)/r, f \cdot (x - 0.5)/r), & \text{if } r_0 < r < r_1 \\ (1, 0, 0), & \text{if } r > r_1 \end{cases}$$

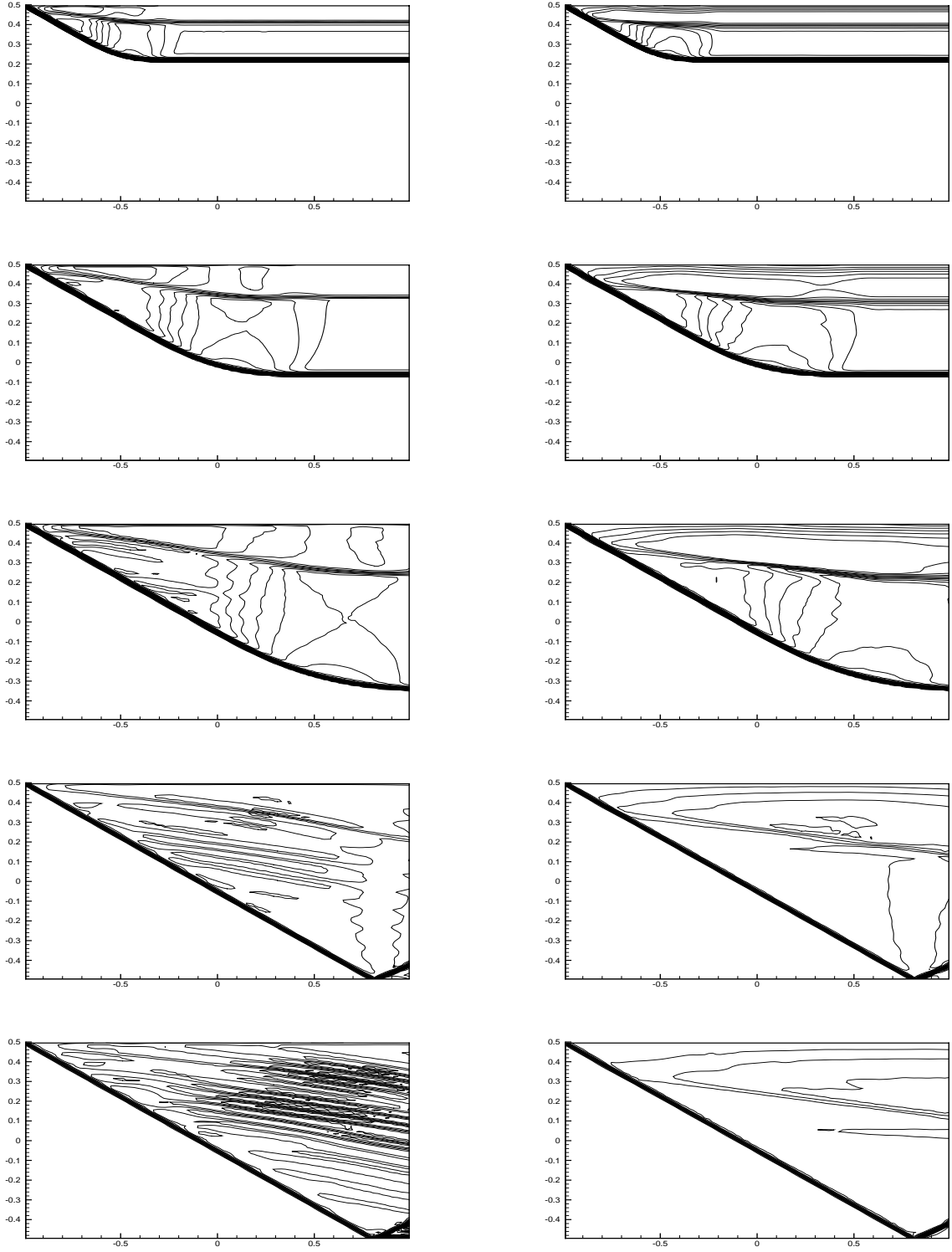


Figure 3.14: Shock reflection. 30 equally spaced contours of ρ at different times on 100×100 mesh with $M = 1$. From top to bottom: $\rho \in [1.03, 1.50]$ at $t = 0.2$, $\rho \in [1.02, 1.52]$ at $t = 0.4$, $\rho \in [1.02, 1.52]$ at $t = 0.6$, $\rho \in [1.05, 1.92]$ at $t = 1.0$, and $\rho \in [1.05, 2.10]$ at $t = 1.4$. Left: P^2 ; right: P^2 -LDF.

where $r_0 = 0.1$, $r_1 = 0.115$, $f = (r_1 - r)/(r_1 - r_0)$, $r = [(x - 0.5)^2 + (y - 0.5)^2]^{1/2}$. Note that the rotor is not in equilibrium, since the centrifugal forces are not balanced. The magnetic field will confine the rotating dense fluid into an oblate shape. Periodic boundary condition is used.

The results at $t = 0.295$ on a 100×100 mesh with $M = 10$ are shown in Figure 3.15, which are the density ρ , pressure p , hydrodynamic Mach number $|\mathbf{u}|/c$ with sound speed $c = \sqrt{\gamma p / \rho}$, and also the magnetic pressure $\mathbf{B}^2/2$. The solution is very well resolved. See the results in [30] for a reference.

Similarly to what the authors of [5] and [30] have observed, when we zoom in the central part of Mach number obtained by using the standard piecewise P^k (left column in Figure 3.16), we see some “distortion” around the central rotating area, for example near the points $(0.40, 0.45)$ and $(0.60, 0.55)$. Besides, we also find some extra features around the points $(0.50, 0.35)$ and $(0.50, 0.65)$. We say these features are “extra” since they are not observed in [5] and [30], nor in our results using the locally divergence-free P^k (right column in Figure 3.16). Moreover, there is no distortion in our locally divergence-free solutions, which are quite comparable with the “good” results in [5] and [30]. This indicates that using the locally divergence-free space can reduce nonphysical features in the computation.

We also plot cuts from Mach number to see the convergence of the methods and the different behavior of the two solution spaces, in Figure 3.17. These cuts are at $x = 0.413$ and $x = 0.545$. It can be seen that the results using locally divergence-free solution space behave better in convergence, and they give relatively smoother solutions.

4 Concluding remarks

Discontinuous Galerkin method using locally divergence-free piecewise polynomial solution spaces seems to be very effective for solving the ideal MHD equations. It could produce results no worse than the ones obtained from the discontinuous Galerkin methods using the standard piecewise polynomial space with the same polynomial degree, yet uses less

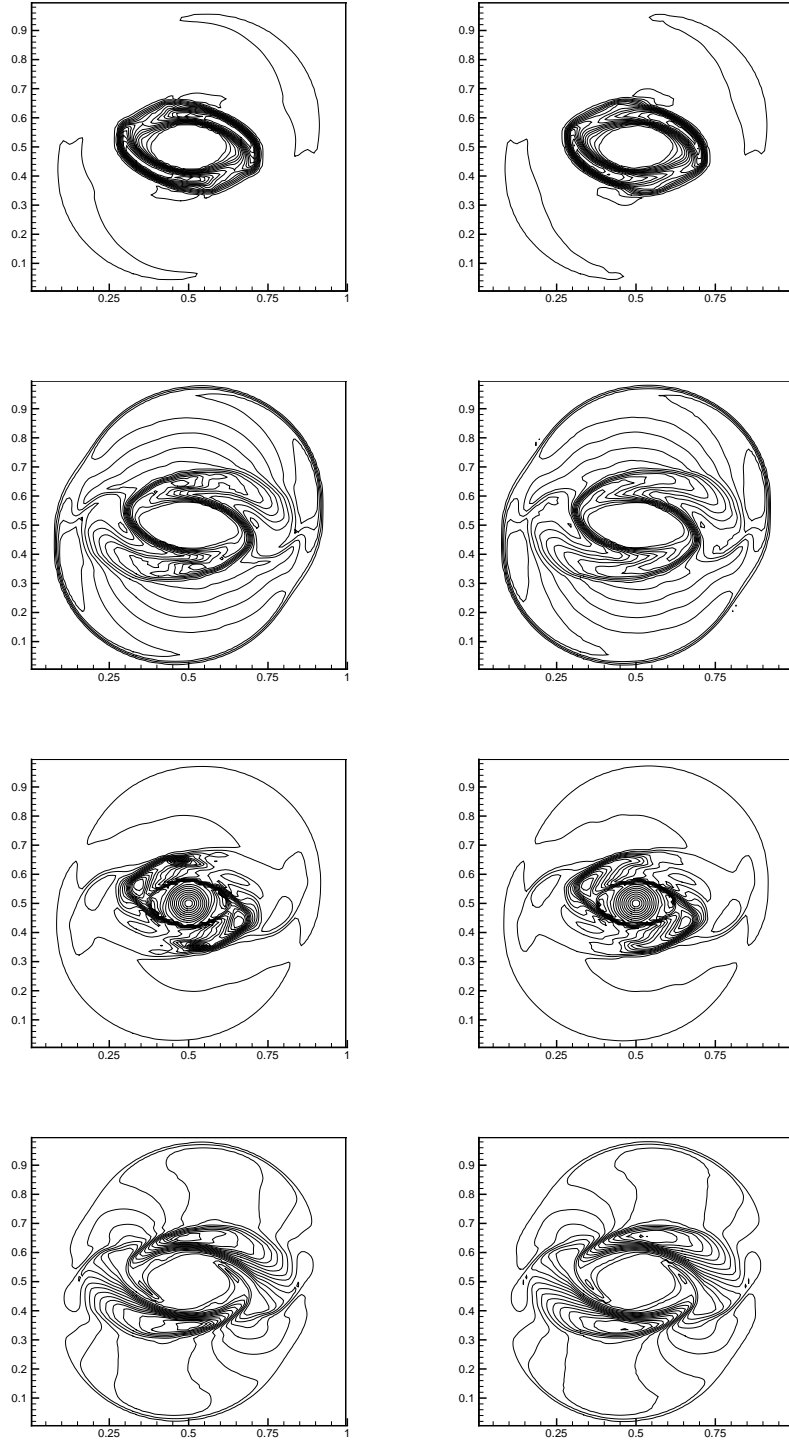


Figure 3.15: Rotor. From top to bottom: 15 equally spaced contours of density $\rho \in [0.730, 7.330]$; pressure $p \in [0.058, 0.733]$; Mach number $|\mathbf{u}|/c \in [0.147, 2.270]$; magnetic pressure $\mathbf{B}^2/2 \in [0.059, 0.655]$. At $t = 0.295$ on 100×100 mesh with $M = 10$. Left: P^2 ; right: P^2 -LDF.

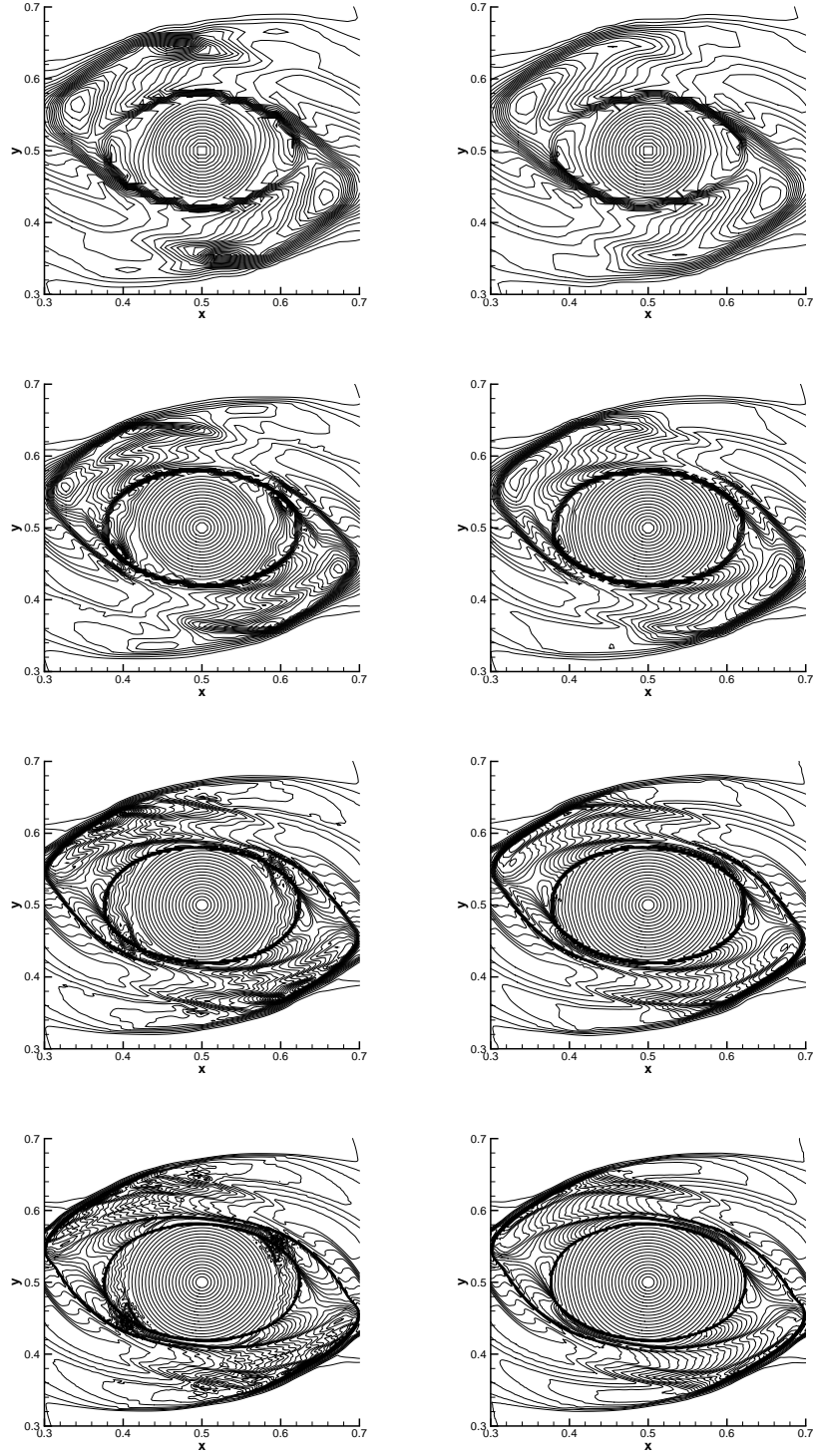


Figure 3.16: Rotor. Zoom-in central part for Mach number. 30 equally spaced contours with range $[0.18, 3.12]$ at $t = 0.295$ with $M = 10$. From top to bottom: 100×100 mesh, 200×200 mesh, 400×400 mesh, 800×800 mesh. Left: P^2 ; right: P^2 -LDF.

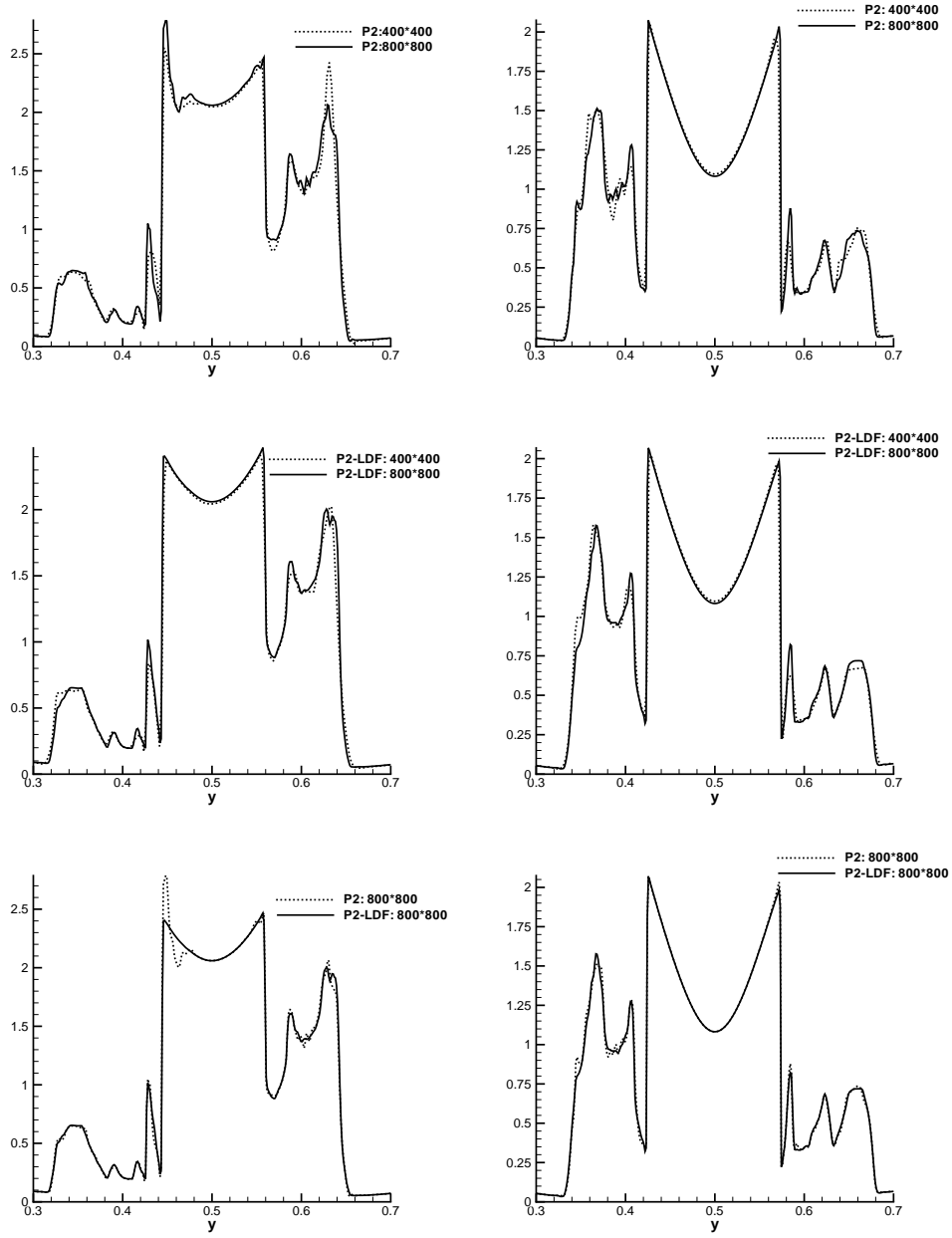


Figure 3.17: Rotors. Cuts of Mach number. Left column: at $x = 0.413$; right column: at $x = 0.545$. The first two rows are for convergence: dotted lines are for 400×400 mesh, solid lines are for 800×800 mesh; the top row is for P^2 , the middle row is for P^2 -LDF. The last row is for comparison of P^2 and P^2 -LDF: dotted lines are for P^2 , solid lines are for P^2 -LDF. $M = 10$.

computational cost. More importantly, this locally divergence-free discontinuous Galerkin method could enhance the numerical stability and reduce some nonphysical features in the solutions.

References

- [1] N. Aslan and T. Kammash, *Developing numerical fluxes with new sonic fix for MHD equations*, Journal of Computational Physics, v133 (1997), pp.43-55.
- [2] G.A. Baker, W.N. Jureidini and O.A. Karakashian, *Piecewise solenoidal vector fields and the Stokes problem*, SIAM Journal on Numerical Analysis, v27 (1990), pp.1466-1485.
- [3] D.S. Balsara, *Divergence-free adaptive mesh refinement for magnetohydrodynamics*, Journal of Computational Physics, v174 (2001), pp.614-648.
- [4] D.S. Balsara, *Second order accurate schemes for magnetohydrodynamics with divergence-free reconstruction*, Astrophysical Journal, to appear.
- [5] D.S. Balsara and D.S. Spicer, *A staggered mesh algorithm using high order Godunov fluxes to ensure solenoidal magnetic fields in magnetohydrodynamic simulations*, Journal of Computational Physics, v149 (1999), pp.270-292.
- [6] J.U. Brackbill and D.C. Barnes, *The effect of nonzero $\nabla \cdot \mathbf{B}$ on the numerical solution of the magnetohydrodynamic equations*, Journal of Computational Physics, v35 (1980), pp.426-430.
- [7] S.H. Brecht, J.G. Lyon, J.A. Fedder and K. Hain, *A simulation study of east-west IMF effects on the magnetosphere*, Geophysical Research Letters, v8 (1981), pp.397-400.
- [8] M. Brio and C.C. Wu, *An upwind differencing scheme for the equations of ideal magnetohydrodynamics*, Journal of Computational Physics, v75 (1988), pp.400-422.

- [9] B. Cockburn, S. Hou and C.-W. Shu, *The Runge-Kutta local projection discontinuous Galerkin finite element method for conservation laws IV: the multidimensional case*, Mathematics of Computation, v54 (1990), pp.545-581.
- [10] B. Cockburn, S.-Y. Lin and C.-W. Shu, *TVB Runge-Kutta local projection discontinuous Galerkin finite element method for conservation laws III: one dimensional systems*, Journal of Computational Physics, v84 (1989), pp.90-113.
- [11] B. Cockburn, F. Li and C.-W. Shu, *Locally divergence-free discontinuous Galerkin methods for the Maxwell equations*, Journal of Computational Physics, to appear.
- [12] B. Cockburn and C.-W. Shu, *The Runge-Kutta discontinuous Galerkin method for conservation laws V: multidimensional systems*, Journal of Computational Physics, v141 (1998), pp.199-224.
- [13] B. Cockburn and C.-W. Shu, *Runge-Kutta Discontinuous Galerkin methods for convection-dominated problems*, Journal of Scientific Computing, v16 (2001), pp.173-261.
- [14] W. Dai and P.R. Woodward *A simple finite difference scheme for multidimensional magnetohydrodynamic equations*, Journal of Computational Physics, v142 (1998), pp.331-369.
- [15] A. Dedner, F. Kemm, D. Kröner, C.-D. Munz, T. Schnitner and M. Wesenberg, *Hyperbolic divergence cleaning for the MHD equations*, Journal of Computational Physics, v175 (2002), pp.645-673.
- [16] C.R. Evans and J.F. Hawley, *Simulation of magnetohydrodynamic flows: a constrained transport method*, Astrophysical Journal, v332 (1988), pp.659-677.
- [17] B.-N. Jiang, J. Wu and L. A. Povinelli, *The origin of spurious solutions in computational electromagnetics*, Journal of Computational Physics, v125 (1996), pp.104-123.

- [18] G.-S. Jiang and C.-C. Wu, *A high-order WENO finite difference scheme for the equations of ideal magnetohydrodynamics*, Journal of Computational Physics, v150 (1999), pp.561-594.
- [19] O.A. Karakashian and W.N. Jureidini, *A nonconforming finite element method for the stationary Navier-Stokes equations*, SIAM Journal on Numerical Analysis, v35 (1998), pp.93-120.
- [20] C.-D. Munz, P. Omnes, R. Schneider, E. Sonnendrücker and U. Voß, *Divergence correction techniques for Maxwell solvers based on a hyperbolic model*, Journal of Computational Physics, v161 (2000), pp.484-511.
- [21] S.A. Orszag and C.-M. Tang, *Small-scale structure of two-dimensional magnetohydrodynamic turbulence*, Journal of Fluid Mechanics, v90 (1979), pp.129-143.
- [22] K.G. Powell, *An approximate Riemann solver for magnetohydrodynamics (that works in more than one dimension)*, ICASE report No. 94-24, Langley, VA, 1994.
- [23] J. Qiu and C.-W. Shu, *Runge-Kutta discontinuous Galerkin method using WENO limiters*, submitted to SIAM Journal on Scientific Computing.
- [24] J. Qiu and C.-W. Shu, *Hermite WENO schemes and their application as limiters for Runge-Kutta discontinuous Galerkin method: one dimensional case*, Journal of Computational Physics, to appear.
- [25] D. Ryu, F. Miniati, T.W. Jones and A. Frank *A divergence-free upwind code for multi-dimensional magnetohydrodynamic flows*, Astrophysical Journal, v509 (1998), pp.244-255.
- [26] C.-W. Shu, *TVB uniformly high-order schemes for conservation laws*, Mathematics of Computation, v49 (1987), pp.105-121.

- [27] C.-W. Shu, *Essentially non-oscillatory and weighted essentially non-oscillatory schemes for hyperbolic conservation laws*, in *Advanced Numerical Approximation of Nonlinear Hyperbolic Equations*, B. Cockburn, C. Johnson, C.-W. Shu and E. Tadmor (Editor: A. Quarteroni), Lecture Notes in Mathematics, volume 1697, Springer, 1998, pp.325-432.
- [28] C.-W. Shu and S. Osher, *Efficient implementation of essentially non-oscillatory shock-capturing schemes*, Journal of Computational Physics, v77 (1988), pp.439-471.
- [29] J.M. Stone and M.L. Norman, *ZEUS-2D: A radiation magnetohydrodynamics code for astrophysical flows in two space dimensions. II The magnetohydrodynamic algorithms and tests*, Astrophysical Journal Supplement Series, v80 (1992), pp.791-818.
- [30] G. Tóth, *The $\nabla \cdot \mathbf{B} = 0$ constraint in shock-capturing magnetohydrodynamics codes*, Journal of Computational Physics, v161 (2000), pp.605-652.
- [31] C.C. Wu, *An Kelvin-Helmholtz instability at the magnetopause boundary*, Journal of Geophysical Research, v91 (1986), pp.3042-3060.
- [32] K.S. Yee, *Numerical solution of initial boundary value problems involving Maxwell's equations in isotropic media*, IEEE Transactions on Antenna Propagation, AP-14 (1966), pp.302-307.